PHYSICAL REVIEW D **94,** 114506 (2016)

Model of random center vortex lines in continuous $2+1$-dimensional spacetime

Derar Altarawneh,[1,*] Michael Engelhardt,[2,†] and Roman Höllwieser[2,3,‡]

[1]*Department of Applied Physics, Tafila Technical University, Tafila 66110, Jordan*
[2]*Department of Physics, New Mexico State University, P.O. Box 30001, Las Cruces, New Mexico 88003-8001, USA*
[3]*Institute of Atomic and Subatomic Physics, Vienna University of Technology, Operngasse 9, 1040 Vienna, Austria*

(Received 6 July 2016; published 9 December 2016)

A picture of confinement in QCD based on a condensate of thick vortices with fluxes in the center of the gauge group (center vortices) is studied. Previous concrete model realizations of this picture utilized a hypercubic space-time scaffolding, which, together with many advantages, also has some disadvantages, e.g., in the treatment of vortex topological charge. In the present work, we explore a center vortex model which does not rely on such a scaffolding. Vortices are represented by closed random lines in continuous $2+1$-dimensional space-time. These random lines are modeled as being piecewise linear, and an ensemble is generated by Monte Carlo methods. The physical space in which the vortex lines are defined is a torus with periodic boundary conditions. Besides moving, growing, and shrinking of the vortex configurations, also reconnections are allowed. Our ensemble therefore contains not a fixed but a variable number of closed vortex lines. This is expected to be important for realizing the deconfining phase transition. We study both vortex percolation and the potential $V(R)$ between the quark and antiquark as a function of distance R at different vortex densities, vortex segment lengths, reconnection conditions, and at different temperatures. We find three deconfinement phase transitions, as a function of density, as a function of vortex segment length, and as a function of temperature.

DOI: 10.1103/PhysRevD.94.114506

I. INTRODUCTION

QCD is the regnant theory of the strong interaction. It is formulated in terms of quarks and gluons, which are the basic degrees of freedom that make up hadronic matter. QCD is well understood in the regime where we have a large momentum transfer (ultraviolet regime). In this regime, the theory is weakly coupled and can thus be solved using perturbative methods. On the other hand, at low energy, analytical solutions are very hard to obtain due to the large coupling constant and the highly nonlinear nature of the strong force. It happens especially in this infrared regime that the QCD vacuum exhibits some extraordinary features, among them the confinement of quarks into bound hadrons and chiral symmetry breaking (χSB), the origin of mass in QCD. A perspective to construct a cogent, comprehensive model of the strong interaction vacuum in which, in particular, a connection between topological properties and confinement can be drawn appeared in the framework of the magnetic (center) vortex picture [1–6]: chromomagnetic flux lines compress the chromoelectric flux between color electric sources into a flux tube (or a "string"), resulting in a linearly rising potential and thus confinement.

In D-dimensional space-time, center vortices are (thickened) $(D-2)$-dimensional chromomagnetic flux degrees of freedom. The center vortex picture of the strong interaction vacuum assumes that these are the relevant degrees of freedom in the infrared sector of the strong interaction; the center vortices consequently are taken to be weakly coupled and can thus be expected to behave as random lines (for $D=3$) or random surfaces (for $D=4$). The magnetic flux carried by the vortices is quantized in units which are singled out by the topology of the gauge group, such that the flux is stable against small local fluctuations of the gauge fields. In the vortex model of confinement, the deconfinement transition results from a percolation transition of these chromomagnetic flux degrees of freedom. This theoretically appealing picture has been buttressed by a multitude of numerical calculations, both in lattice Yang-Mills theory and within a corresponding infrared effective model, see, e.g., Refs. [7–20], or Ref. [21], which summarizes the main features. Recent results [22] have also suggested that the center vortex model of confinement is more consistent with lattice results than other currently available models. Lattice studies further indicate that vortices may also be responsible for topological charge [23–31] and χSB [32–45] and thus unify all nonperturbative phenomena engendered by

*derar@ttu.edu.jo
†engel@nmsu.edu
‡hroman@kph.tuwien.ac.at

the structure of the strong interaction vacuum in a common framework.

A concrete implementation of the vortex picture, using a hypercubic lattice scaffolding to support the random vortex lines or surfaces, has been studied extensively by one of the authors [12,15,24,25,36,46–49]. The hypercubic formulation has a number of advantages, among them simple Monte Carlo updates which naturally include surfaces fusing and disassociating, and a straightforward bookkeeping of vortex location, permitting, e.g., simple evaluation of Wilson loops and counting of vortex surface intersections. On the other hand, however, this formulation has revealed weaknesses as far as the calculation of topological charge is concerned. Vortex world-surface configurations in this formulation, being restricted to only six discrete space-time directions in which they can extend, exhibit ambiguities in the definition of topological charge which would not appear in ensembles of arbitrary two-dimensional surfaces in continuous four-dimensional space-time.

In view of this, we explore in the present work an alternative formulation, which avoids the shortcomings of the hypercubic construction, concentrating in a first step on a model of random flux lines in $D = 2 + 1$ space-time dimensions, representing vortices of the $SU(2)$ gauge group (i.e., there are no branchings of the vortex lines [12,15]). The lines are composed of straight segments connecting nodes randomly distributed in three-dimensional space. Allowance is made for nodes moving as well as being added or deleted from the configurations during Monte Carlo updates. Furthermore, Monte Carlo updates disconnecting and fusing vortex lines; i.e., reconnection updates are implemented. Given that the deconfining phase transition is a percolation transition, such processes play a crucial role in the vortex picture. The model is formulated in a toroidal finite volume, with periodic boundary conditions, which allows for a study of finite temperatures (via changes in the temporal extent of the volume). The resulting vortex ensemble is used, in particular, to evaluate the string tension and its behavior as a function of temperature, with a view toward detecting the high-temperature deconfining phase transition.

The above scheme of modeling random lines (and higher-dimensional manifolds) is reminiscent of models employed in the study of quantum gravity [50–55]. While the present work focuses only on the lowest-dimensional case, the inclusion of a variable number of (vortex) clusters in the ensemble is a feature that is not generally contemplated in quantum gravity applications. Here, it is crucial in order to include the physics of the deconfinement transition. Also, the use of a torus with periodic boundary conditions, on which the vortices are defined, in order to treat finite temperature, constitutes a significant complication. The realization of the vortex model in continuous space-time keeps spatial rotational symmetry intact. Hence, the model allows us to measure rotationally invariant potentials, correlators, or string tensions. One concrete example where rotational invariance would constitute an asset is the study of the baryonic potential, where the existing work within the hypercubic construction [47] required a thorough analysis of the angular dependence of the string tension to obtain a correct interpretation of the results. In general, physical questions that require using off-axis directions can be treated better; for example, the model presented here has already been used to study catenary solutions for meson-meson correlators represented by circular Wilson loops [20], in which case the analysis becomes truly one dimensional, without any cubic artifacts in the way the minimal surface forms. Having continuous degrees of freedom, however, requires a number of model parameters to restrict, e.g., the vortex density, and precise fine-tuning of these parameters is necessary. Hence, we will start by introducing the modeling details in Sec. II and discuss all the parameters. In Sec. III, we explain the observables we analyze in this paper, and results will be presented and discussed in Sec. IV. Section V provides a summary of the main results and a short outlook.

II. MODEL DESCRIPTION

In the model, vortices are represented by closed random lines in $2 + 1$-dimensional (Euclidean) space-time. Since vortices of the $SU(2)$ gauge group are being modeled, there are no branchings of the vortex lines. The physical space in which the vortex lines are defined is a torus $L_S^2 \times L_T$ with "spatial" extent L_S, "temporal" extent L_T, and periodic boundary conditions in all directions. The random lines are modeled as being piecewise linear between "nodes" with vortex segment length L restricted to a certain range $L_{\min} < L < L_{\max}$. This range sets a scale of the model; for practical reasons, we choose a scale of $L \approx 1$, i.e., $L_{\min} = 0.3$ and $L_{\max} = 1.7$ in appropriate units. Within this paper, we use volumes with $L_S = 16$, where finite size effects are under control (see Sec. IV E), and varying time lengths L_T. Variations of the vortex segment length ranging away from the aforementioned range will also be examined. An ensemble is generated by Monte Carlo methods, starting with a random initial configuration. A Metropolis algorithm is applied to add, move, and delete nodes using the action

$$S = \alpha L + \gamma \varphi^2, \tag{1}$$

with action parameters α and γ for the vortex segment length L and the vortex angle φ at nodes, respectively. At a given (current) node, the vortex segment length L is defined to be the distance to the previous node, and the vortex angle is the angle between the oriented vectors of the vortex lines connecting the previous, current, and next nodes; see Fig. 1. This type of action, penalizing both vortex length and curvature, is analogous to the action used in previous

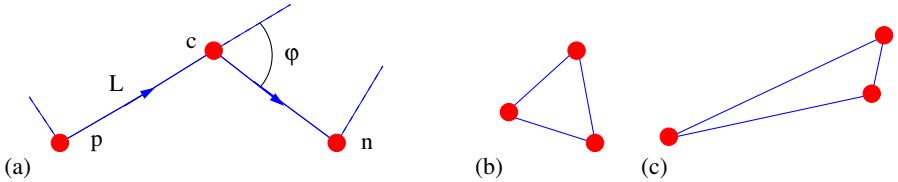

FIG. 1. (a) The action $S = \alpha L + \gamma\varphi^2$ of the current node (c) is given by the vortex length L to the previous node (p) and the angle φ between the vortex lines to the previous (p) and the next node (n). Three node clusters of shape (b) are more likely accepted by the Metropolis algorithm than of shape (c).

hypercubic lattice models [12,15]. Furthermore, when two vortices approach each other, they can reconnect or separate at a bottleneck, as described in detail further below. The ensemble therefore will contain not a fixed but a variable number of closed vortex lines or "vortex clusters." This is expected to be important for realizing the deconfining phase transition. Moreover, new (three-node) clusters are permitted to "pop out" of the vacuum at random positions, again governed by the above action, and hence, a small equilateral triangle is more probable than a long acute triangle; see Fig. 1. The new cluster then evolves further in subsequent updates, along with all other clusters. Also, the reverse process, annihilation of a three-node cluster, is possible; it occurs when a node is deleted from a three-node cluster, leading to a two-node cluster. Such a cluster is equivalent to the absence of any flux and is therefore deleted completely.

In the following, we discuss the individual updates and parameters of the model in more detail.

A. Move, add, and delete

Move, add, and delete updates are applied to the vortex nodes via the Metropolis algorithm; i.e., the difference of the action of the affected nodes before (S_i) and after (S_f) the update determines the probability $P = \min(1, \exp(S_i - S_f))$ of the update being accepted. The move update attempts to move the current node by a random vector of maximal length $r_m = 4L_{\min}$; it affects the action of three nodes, the current node itself, and its neighbors; see Fig. 2.

The add update attempts to add a node at a random position within a radius $r_a = 3L_{\min}$ around the midpoint between the current and the next node; see Fig. 3. The action S_i before the update is given by the sum of the action at the current and the next node, while the action S_f after the update is the sum of the action at the current, the new, and the next nodes. Conversely, deleting the current node affects three nodes, i.e., the previous, the current, and the next node before the update and only two nodes (previous and next) after the update; see Fig. 4. Therefore, the probability P for the add update is in general much smaller than for the delete update; the vortex structure tends to vanish quickly if both updates are tried equally often. As detailed below, add updates were attempted at a significantly larger rate than delete updates.

In general, move, add, and delete updates can come into conflict with the restricted range of allowed vortex segment lengths L. In early implementations, the move update was applied to every node of the configuration, and if the resulting vortex segment lengths conflicted with the allowed range, the corresponding nodes were deleted, or auxiliary ones at midpoints were added, respectively. In principle, in this scheme, the configuration can be stabilized for a set of fine-tuned parameters, but these parameters lead to very dense vortex configurations deep in the confinement phase. Hence, in order to explore the whole phase space of the model, an additional density parameter ρ is introduced, restricting the number of nodes in a certain volume. The add update is rejected if the number of nodes within a $3 \times 3 \times 3$ volume around the new node exceeds the density parameter ρ. Also, new clusters popping up are subjected to this density cutoff; i.e., the number of nodes in a $3 \times 3 \times 3$ volume has to be less than $\rho - 3$ for a three-node cluster to pop up there. Further, all updates resulting in vortex segment lengths L out of the range

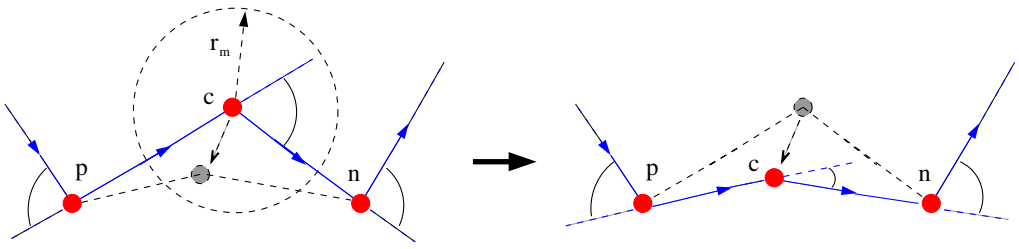

FIG. 2. The movement of the current node (c) within a certain range r_m is affecting the connected vortex lines and the angles at the current (c), the previous (p), and the next node (n).

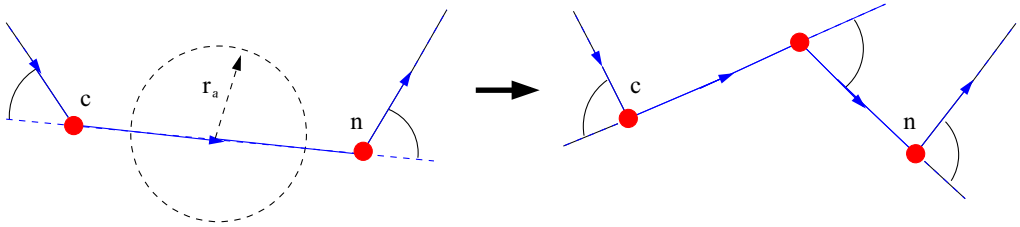

FIG. 3. The add update adds a node after the current node (c) within a range r_a around the midpoint of the vortex line to the next node (n). Two vortex angles before and three after the update are affected, and one vortex line is split into two.

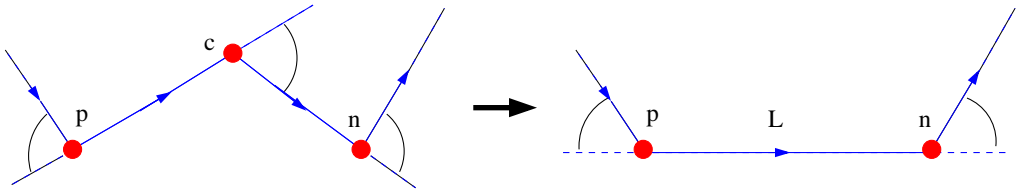

FIG. 4. The delete update deletes the current node (c), joining the connected vortex lines into one between the previous (p) and the next node (n). It affects three and two vortex angles before and after the update, respectively. The new vortex length L has to lie in the range $L_{\min} < L < L_{\max}$, like for all other updates.

$L_{\min} < L < L_{\max}$ are also rejected. The update strategy is randomized to move a node in two out of three cases (66%) and apply the add update about five times more often than the delete update (28% vs 6%). Maximal movement and add "radii" r_m and r_a are set to, respectively, four and three times $L_{\min}$. The different parameters and restrictions in the model may seem artificial at first sight, but they are optimized in order to guarantee a balance between action and entropy of the system. The influence of the individual parameters on the model and their "physical" effect to favor either action or entropy will be discussed in Sec. IV. An overview of all parameters and the Monte Carlo sweep will be given in Secs. II C and II D, respectively, but before this, a detailed discussion of the reconnection update, which is applied after every move and add update, is in order.

B. Reconnections

If the current node is not deleted, all nodes in a $3 \times 3 \times 3$ volume around the current node are considered for reconnections. The reconnection update causes the cancellation of two close, parallel vortex lines and reconnection of the involved nodes with new vortex lines. Physically, this implements the fact that two vortex lines lying on top of one another is equivalent to no physical flux being present; since the actual vortices being represented are considered to possess a certain thickness, the cancellation can be considered to occur as soon as the vortices significantly overlap, i.e., are sufficiently close and parallel. The terms "close" and "parallel" call for two more parameters in the model, the reconnection length r_r and the reconnection angle ϵ. The shortest distance and the angle between two vortex lines must be smaller than r_r and ϵ, respectively, in order to reconnect the four involved nodes with new vortex lines. An illustrative example of the reconnection update is shown in Fig. 5. The lengths of the new vortex lines, as always, have to be smaller than $L_{\max}$; however, the constraint of minimal distance $L_{\min}$ is not enforced in reconnection updates in order to allow for reconnections of almost congruent vortex lines. If all conditions for the reconnection are fulfilled, the update is subjected to the

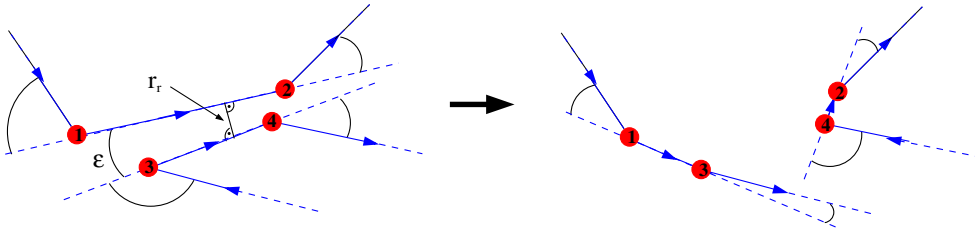

FIG. 5. The reconnection update deletes the vortex lines between nodes 1-2 and 3-4 and reconnects nodes 1-3 and 4-2. The plot shows the affected vortex angles, the reconnection angle ϵ and distance r_r. The plotted vortex lines/nodes might belong to the same or different clusters. Note that the orientation of some vortex lines was reversed in this example, cf. the main text.

Metropolis algorithm, considering the action of the four nodes involved. The reconnection update allows separation and merging of vortex clusters. It should be noted that the data structure of the vortex nodes imposes an orientation on the vortex clusters (previous, next, etc.). If two merging clusters have opposite orientation, the orientation of one of the clusters is reversed, cf. Fig. 5. This orientation is a technical issue only and has no physical meaning in this model.

C. Parameters

This section summarizes all parameters used in the model and the optimized values used for the simulations on $16^2 \times L_T$ volumes. It should be noted that the search for viable parameter sets and update conditions constituted the most demanding part of the simulation effort in this work. This includes tuning for useful acceptance rates for move, add, delete, and reconnection updates as well as new clusters popping up out of the vacuum. In addition, a substantive competition between action and entropy in the ensemble must be maintained to obtain physically interesting behavior. The action, $S = \alpha L + \gamma\varphi^2$, penalizes both vortex length and curvature (via the angles between vortex segments) and thus mimics the first two terms of a systematic gradient expansion of the generic action associated with a line:

(i) Vortex length action parameter $\alpha = 0.11$:
The vortex segment length L at a node is defined as the distance to the previous node.

(ii) Vortex angle action parameter $\gamma = 0.33$:
The vortex angle φ is defined as the angle between the oriented vectors of the vortex lines connecting the previous, current, and next nodes; see Fig. 1.

(iii) Minimal vortex segment length $L_{\min} = 0.3$:
This parameter acts as a minimal length scale in the model, also determining
(a) the maximal radius of the move update $r_m = 4L_{\min}$; see Fig. 2.
(b) the maximal radius of the add update $r_a = 3L_{\min}$; see Fig. 3.
(c) the reconnection length $r_r = L_{\min}$; see Fig. 5.

(iv) Recombination angle $\epsilon = 5°$:
ϵ is the maximal angle between recombining vortex lines; see Fig. 5.

(v) Vortex density cutoff $\rho = 8$:
Maximal number of nodes in a $3 \times 3 \times 3$ volume.

(vi) Maximal vortex segment length $L_{\max} = 1.7$

$L_{\min} = r_r$, ϵ, and ρ are all manifestations of the vortex thickness, which determines the ultraviolet limit of validity of the vortex picture. Two coinciding $SU(2)$ vortex fluxes are equivalent to the vacuum, since they contribute a trivial unit factor to any Wilson loop. Now, if the vortices have a certain thickness, then already two approximately parallel vortices sufficiently close to one another are, in substance, equivalent to the vacuum; in a sense, they annihilate. This has a number of consequences, encoded in the aforementioned parameters. For one, vortices cannot be packed arbitrarily closely; only a certain maximal density is viable without annihilation. This is encoded in the parameter ρ; in implementations of the vortex model employing a hypercubic scaffolding, the analogous parameter is simply the lattice spacing. Furthermore, the vortex lines of the model cannot fluctuate on scales much smaller than the vortex thickness; it makes no sense to think of a rapidly fluctuating line defining the center of a thickened vortex structure. Any such fluctuation is smeared out by the thickening and cannot be resolved. This is encoded in the parameter $L_{\min}$. Also, a reconnection update consists, essentially, of an annihilation of two sufficiently coincident vortex segments. For this, they have to be sufficiently parallel, as encoded in ϵ, and sufficiently close to one another, as encoded in $r_r = L_{\min}$. This, again, is a manifestation of vortex thickness, which determines how close and how parallel vortices have to be to be regarded as annihilating.

Finally, the vortex ensemble also depends on the maximal vortex segment length parameter $L_{\max}$. It arises for a technical reason, namely, because the simple manner in which vortex density is limited via the parameter ρ has a shortcoming: the latter limits the density of nodes, not vortex line density itself, and thus there is still the possibility for the system to attain a spuriously high line density by forming long vortex segments, even if the node density is low. To preclude the formation of such a high line density state, which would be favored by entropy, it is necessary to limit also the vortex length per node, i.e., introduce the auxiliary parameter $L_{\max}$. This somewhat artificial implementation is motivated by considerations of practicality; $L_{\max}$ would be superfluous in the presence of a more sophisticated construction limiting vortex line density directly. A related issue arising at finite temperatures, also resolved by the introduction of $L_{\max}$, is the following: if one were to allow long vortex line segments, these could wind around the torus in the temporal direction multiple times. Each subsequent winding would roughly coincide with previous windings, and the windings should therefore annihilate in pairs. This situation is generally not properly recognized by the reconnection step of our algorithm, again permitting the formation of a spuriously high vortex line density that would not arise in a more sophisticated construction which properly detects all relevant annihilations. The introduction of $L_{\max}$ likewise limits this effect in a simple, *ad hoc* manner.

D. Monte Carlo algorithm

For a simulation, the following algorithm was executed a total number of $n_r = n_w + n_m * n_s$ times, where $n_w = 10^4$ is the number of equilibration iterations, $n_m = 2\ldots5 \times 10^5$ is the number of measurements, and $n_s = 10$ the number of sweeps between the measurements:

(i) The Metropolis algorithm for one three-node cluster pop-up is called before the node updates; therefore, the new nodes will also be updated before any measurement.
(ii) Monte Carlo sweep over all nodes in the configuration:
  (a) Metropolis move, add, or delete updates are applied to the nodes with rates 66%, 28%, and 6%.
  (b) If a node is not deleted, possible reconnections are considered.
(iii) After the $n_w = 10^4$ equilibration iterations are complete, measurements are performed separated by $n_s = 10$ Monte Carlo sweeps.

The next section introduces the observables measured in the model.

III. OBSERVABLES

The most directly accessible observables in the model are ones associated with the action used to generate the ensemble, e.g., the total action itself and the actual vortex density. These were used to analyze the equilibration phase of the simulations. A number of $n_w = 10^3$ equilibration sweeps was seen to be generally sufficient for the model to thermalize; however, for the following simulations, $n_w = 10^4$ thermalization steps were used. After that, the average action per node, the actual vortex density, the average vortex segment length and angle, and Wilson loops were measured, and a vortex cluster analysis was performed, every $n_s = 10$ Monte Carlo sweeps. Wilson loop and vortex cluster measurements will be detailed below. The vortex density is a nontrivial observable since the cutoff parameter ρ is applied only for the add update; the vortex node density can locally exceed this cutoff since the vortex nodes can move without density restrictions. The actual vortex density is then given by the node density times the average vortex segment length.

A. Vortex cluster analysis

The vortex cluster analysis comprises counting the number of closed vortex clusters, the number of vortex nodes/line segments for each cluster, the cluster size or maximal extent of each cluster, and the number of clusters winding around the time dimension. The distribution of vortex flux into clusters of different sizes will be visualized in cluster size histograms binning vortex nodes into 20 bins corresponding to the sizes of the clusters to which they belong, where the cluster size is normalized using the maximal possible cluster size s_m. Taking into account the periodic boundary conditions, the maximal possible cluster size is determined by $s_m^2 = L_S^2/2 + L_T^2/4$. In the following analysis, the expression "maximal cluster fraction" will refer to the fraction of vortex nodes/line segments which reside within a cluster of size s_m, i.e., the magnitude of the bin of maximal possible cluster size in the aforementioned histograms. This quantifies to what extent vortices percolate. On the other hand, vortex clusters winding around the time dimension are important in particular in the deconfined phase; in the percolation transition separating the confining and the deconfined phase, the large percolating clusters of the confining phase decay into many such winding clusters [12]. The latter are instrumental in maintaining a spatial string tension in the deconfined phase, while the physical string tension extracted from temporal Wilson loops vanishes [12]. Monitoring in particular vortices winding around the time dimension therefore provides an additional diagnostic for the deconfining transition. Such vortices can be produced during reconnection updates, either in pairs or even singly if the temporal extent of the torus is sufficiently small ($L_T < 3L_{\max}$).

B. Wilson loops

The Wilson loop $W(R,T)$ along a closed rectangular path in space and time of dimensions $R \times T$ is the observable most frequently used to discuss confinement in lattice gauge theory. It can be interpreted in terms of the creation of a static quark-antiquark pair with a certain spatial separation R, its evolution for a time T, and its subsequent annihilation. The effective action associated with this process yields the potential energy contained in the static quark-antiquark pair. Center vortices have a characteristic effect on Wilson loops; each center vortex linked with a Wilson loop (or, equivalently, piercing any area spanned by the loop) contributes a multiplicative factor to the loop corresponding to a center element of the gauge group. This can, indeed, be viewed as the defining property of a center vortex; it specifies the flux carried by the vortex, which is measured by a Wilson loop encircling it. In the case of the $SU(2)$ gauge group considered here, the only nontrivial center element is -1; this is the factor by which any Wilson loop linked to a vortex is multiplied.

To evaluate Wilson loops in the present model, it is sufficient to examine all vortex line segments in a configuration, determining whether each line segment pierces the planar area spanned by the Wilson loop in question and supplying a factor -1 to the Wilson loop for each piercing [if there are no piercings, $W(R,T) = 1$]. Using the fact that larger Wilson loops are simply given by products of smaller Wilson loops with which the larger loop can be tiled, one can organize the calculation of a large number of Wilson loops on a given configuration efficiently. The expectation value of the timelike Wilson loops $\langle W(R,T)\rangle$ yields the quark-antiquark potential,

$$V(R) = -\lim_{T\to\infty} \ln\langle W(R,T)\rangle/T. \tag{2}$$

To extract the string tension σ of the system, an ansatz $V(R) = \sigma R + C/R + V_0$ is fitted to the potentials. The

spatial string tension σ_s is obtained from spatial Wilson loops using Creutz ratios,

$$\chi(R) = -\ln\left(\frac{\langle W(R,R)\rangle\langle W(R+1,R+1)\rangle}{\langle W(R+1,R)\rangle\langle W(R,R+1)\rangle}\right) \xrightarrow{R\to\infty} \sigma_s. \quad (3)$$

The spatial string tension is expected to be correlated with the number of vortex clusters winding in time direction, since these vortices will pierce the spatial Wilson loops.

IV. RESULTS AND DISCUSSION

A. Finite temperature phase transition from varying temporal extent L_T

In this section, we study center vortex ensembles at different temperatures. The following results were obtained on volumes $16^2 \times L_T$ for a range of inverse temperatures L_T in order to resolve the deconfining phase transition at different vortex density cutoffs $\rho = 4$, 6, 8, 10, and 12, with $L_{\max} = 1.7$ and $L_{\min} = 0.3$. In Fig. 6, we show the results extracted for $\rho = 4$, namely, the cluster size histogram, the potential $V(R)$ between the quark and antiquark, and the spatial and temporal string tensions as well as the maximal cluster fraction as a function of temperature. For densities $\rho = 6 - 12$ we show the cluster size histograms in Fig. 8. String tensions and maximal cluster fractions vs. temperature are plotted in Fig. 9. In the $\rho = 4$ case (Fig. 6), we observe a phase transition in the vicinity of the inverse temperatures $L_T = 5$, 6. The cluster size histogram in Fig. 6(a) shows no cluster percolating through the physical volume for $L_T = 4$, whereas from $L_T = 7$ onward, one large percolating cluster starts to dominate the configuration. The quark-antiquark potential shown in Fig. 6(b) is still flat (asymptotically) for $L_T = 5$, while a linearly rising behavior is evident by $L_T = 9$. In between, the potentials do not show a clear linear behavior, and the determination

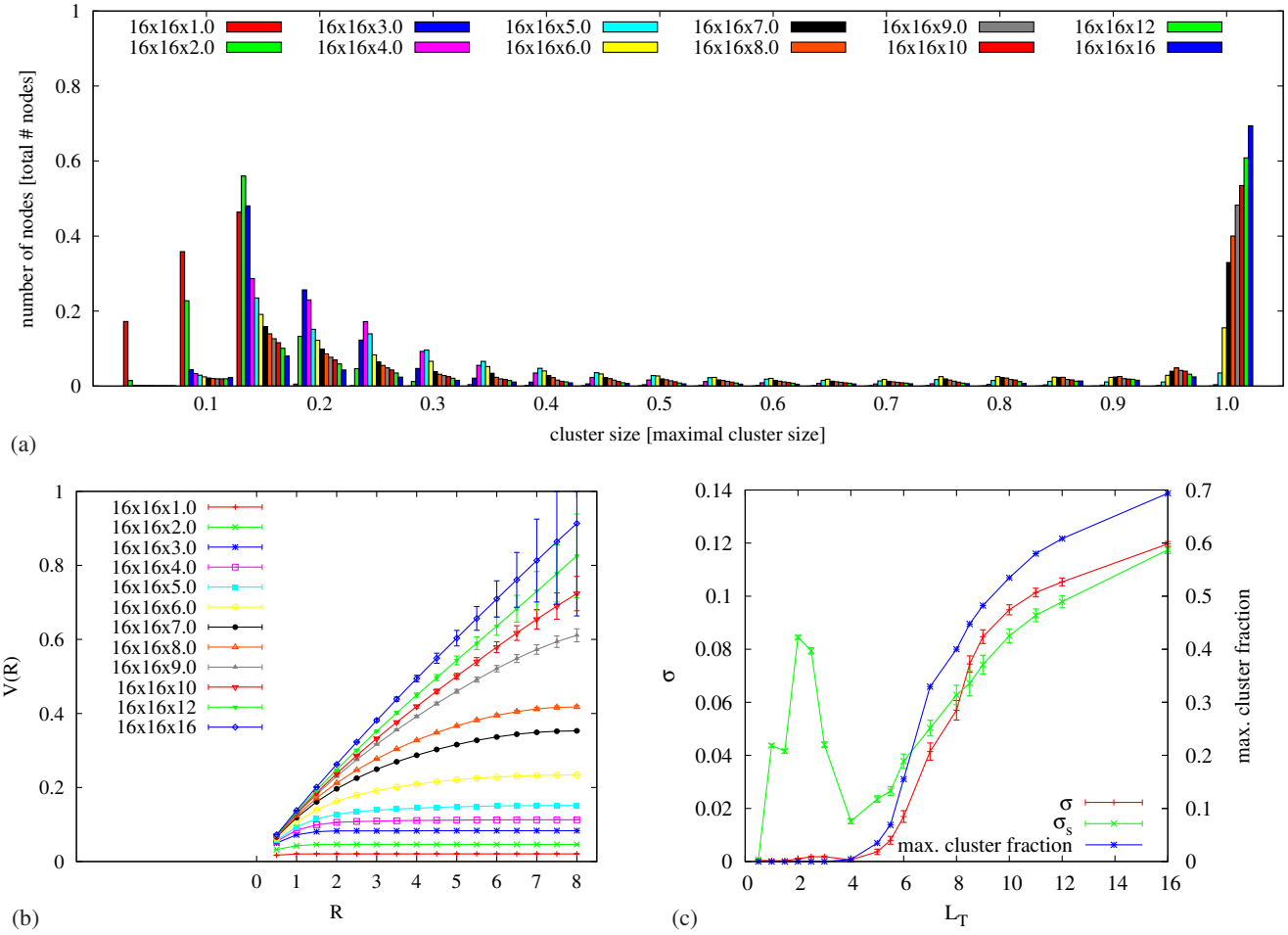

FIG. 6. (a) Cluster size histogram, elucidating the percolation properties of the vortex structure: at high temperatures (small temporal lattice size, e.g., 16^2x1, 2 or 3), we find mainly small vortex clusters (histogram peaks on the left side), whereas for lower temperatures, most of the vortex material is found in clusters of maximal size (right peak), i.e., clusters percolating through the whole lattice. (b) quark-antiquark potentials and (c) maximal cluster fraction (i.e., the fraction of vortex material in clusters of maximal size, the right peak of the histogram plot), temporal and spatial string tensions σ and σ_s for $16^2 \times L_T$ volumes, density cutoff $\rho = 4$, and vortex lengths $L_{\max} = 1.7$, $L_{\min} = 0.3$.

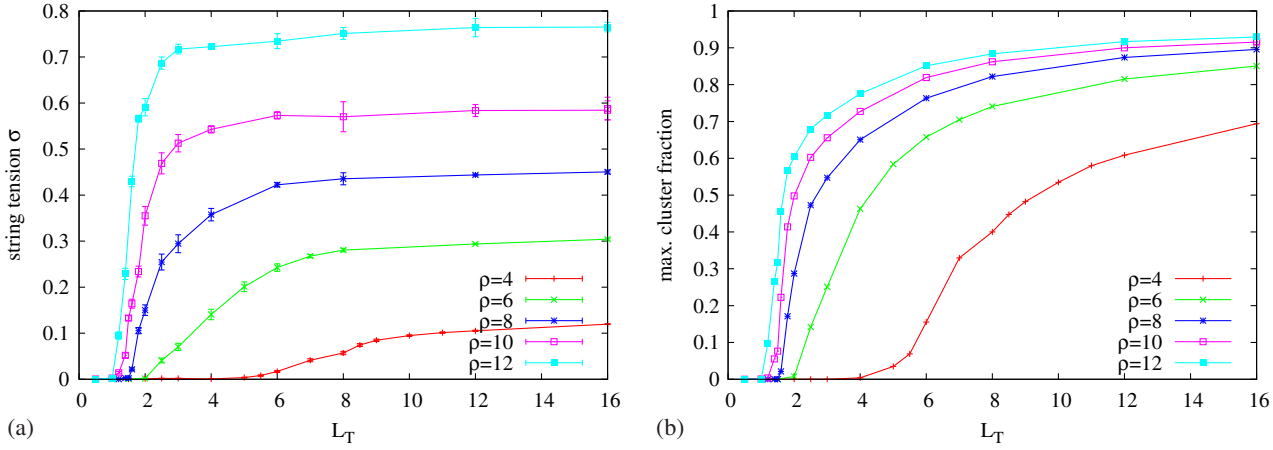

FIG. 7. (a) String tension σ and maximal cluster fraction vs. time extent L_T for different vortex densities ρ on $16^2 \times L_T$ volumes with vortex lengths $L_{\max} = 1.7$ and $L_{\min} = 0.3$.

of the string tension is somewhat ambiguous; however, a deviation of the potential below an exactly linear behavior is to be expected in view of the finite spatial extent of the physical volume and the periodic boundary conditions. In the $\rho = 4$ case, thus, the deconfining transition is not very sharply defined; this is associated with the rather small density cutoff ρ, as is revealed by examination of higher values of ρ.

For higher vortex densities, the phase transition becomes much sharper, and the inverse critical temperature tends to smaller temporal extents L_T. This can be seen in Fig. 9 and especially Fig. 7, which summarizes the results on the finite temperature phase transition for various vortex density cutoffs ρ, and also in the corresponding cluster size histograms in Fig. 8 where one should note the different coloring and temperatures for the individual plots. We locate the phase transition for $\rho = 6$ in the vicinity of $L_T = 2$, for $\rho = 8$ in the vicinity of $L_T = 1.6$, for $\rho = 10$ in the vicinity of $L_T = 1.5$, and for $\rho = 12$ in the vicinity of $L_T = 1.2$. Further, we notice that Fig. 6(c) and the plots in Fig. 9 show a perfect agreement between the confinement (string tension) and percolation (maximal cluster fraction) transitions. In Fig. 11, we show sample configurations for various temperatures and density cutoff $\rho = 4$. While for $L_T = 2$ and 4 [Figs. 11(a) and 11(b)] we see many small vortex clusters, we observe already one big cluster extending over the whole physical volume together with some small clusters for $L_T = 8$ [Fig. 11(c)] while for $L_T = 16$ [zero temperature, Fig. 11(d)], it appears as though almost all nodes were connected. In fact, the careful observer can still make out a few three- and four-node clusters, e.g., at the bottom left corner of the 3D plot in Fig. 11(d), and indeed we still have around 25–30 individual clusters in this configuration; see Fig. 10 for the average number of clusters within a configuration at different inverse temperatures L_T and vortex densities ρ. Nevertheless, the majority [$\approx 70\%$; see Figs. 6(a) and 6(c)] of nodes in Fig. 11(d) is part of one big cluster percolating through the whole physical volume, indicating a confined phase.

It remains to discuss the spatial string tension, which at first sight seems to display unusual behavior in Figs. 6(c) and 9. Apart from the fact that the behavior at very small L_T becomes unphysical, because the lower bound on the vortex segment length $L_{\min}$ artificially suppresses vortices winding around the time direction, one would expect that the spatial string tension remains more or less constant across the deconfining transition; after all, spatial Wilson loops will still be pierced by vortex clusters winding in the time direction even once the percolation effect ceases. However, it appears that these two effects to a certain extent disentangle and are separated as a function of L_T. For $\rho = 4$, we clearly see a decreasing spatial string tension with increasing temperature, in accordance with loss of percolation in the vicinity of the percolation transition, while only below $L_T = 4$, (i.e., above the transition temperature) the effect of winding vortices sets in. Note that (much weaker) hints of such behavior are also seen in vortex ensembles extracted from lattice Yang-Mills configurations [10]. In Fig. 10(b), we plot the number of vortices winding around the time direction; the correlation of these windings with the behavior seen in the spatial string tension for $\rho = 4$ is clearly visible. For higher densities, percolation and winding effects become more entangled and harder to distinguish.

Examining once more Fig. 10, we observe that the total number of vortex clusters peaks around the deconfinement temperature in all cases. This peak is rather weak for $\rho = 4$, but becomes stronger as ρ is allowed to rise. The behavior of the plots in Fig. 10 converges with rising ρ; only the $\rho = 4$ case is fairly strongly separated from the ones at higher ρ. By $\rho = 8$, the behavior of the vortex configurations appears to have converged, and the finite temperature transition seen in Fig. 7 has become sharp. For this reason, we choose $\rho = 8$ for the analysis of the dependence on vortex segment length range in Secs. IV C and IV D.

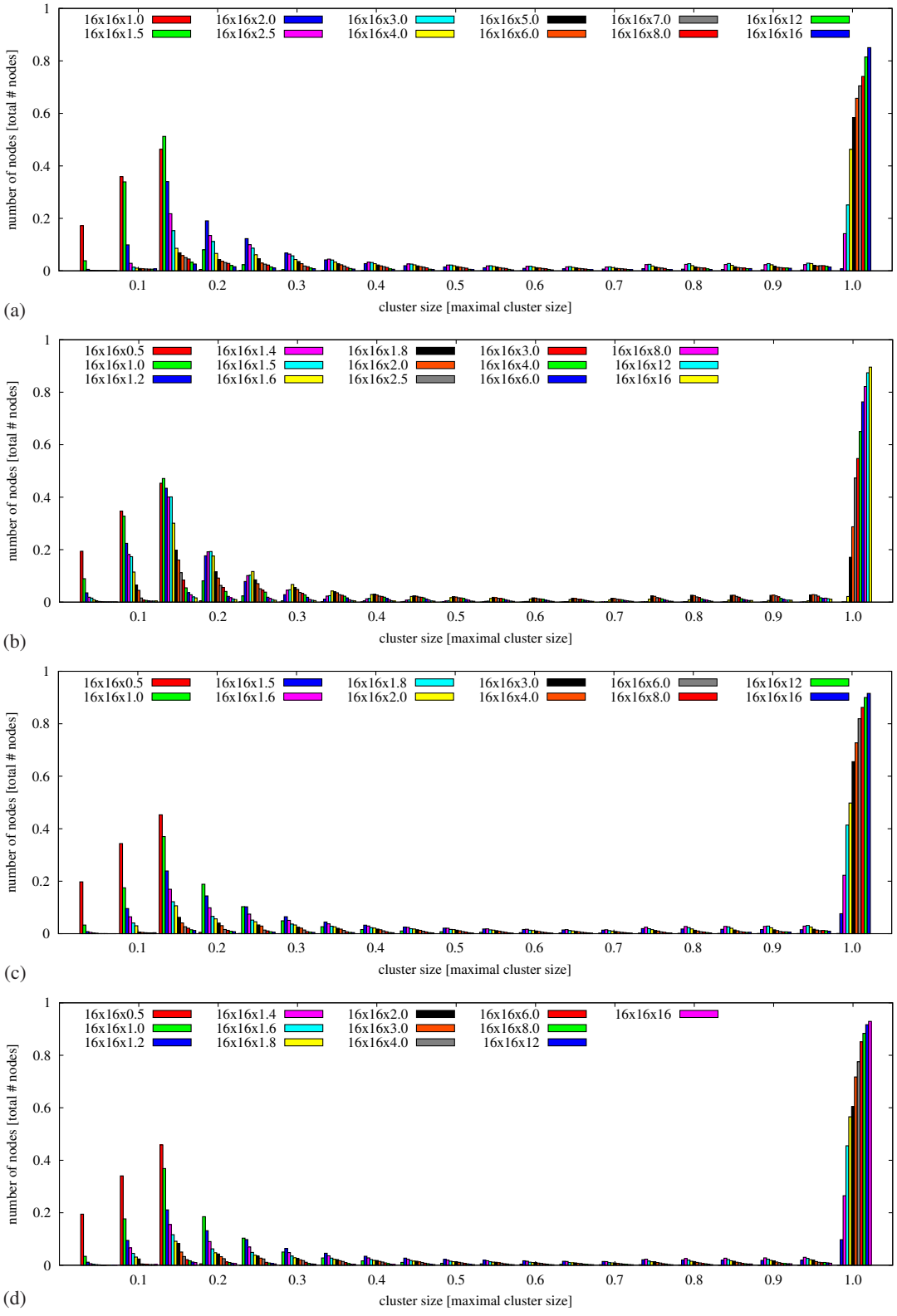

FIG. 8. Cluster size histogram for density cutoff (a) $\rho = 6$, (b) $\rho = 8$, (c) $\rho = 10$, (d) $\rho = 12$ on $16^2 \times L_T$ volumes with vortex lengths $L_{\max} = 1.7$ and $L_{\min} = 0.3$.

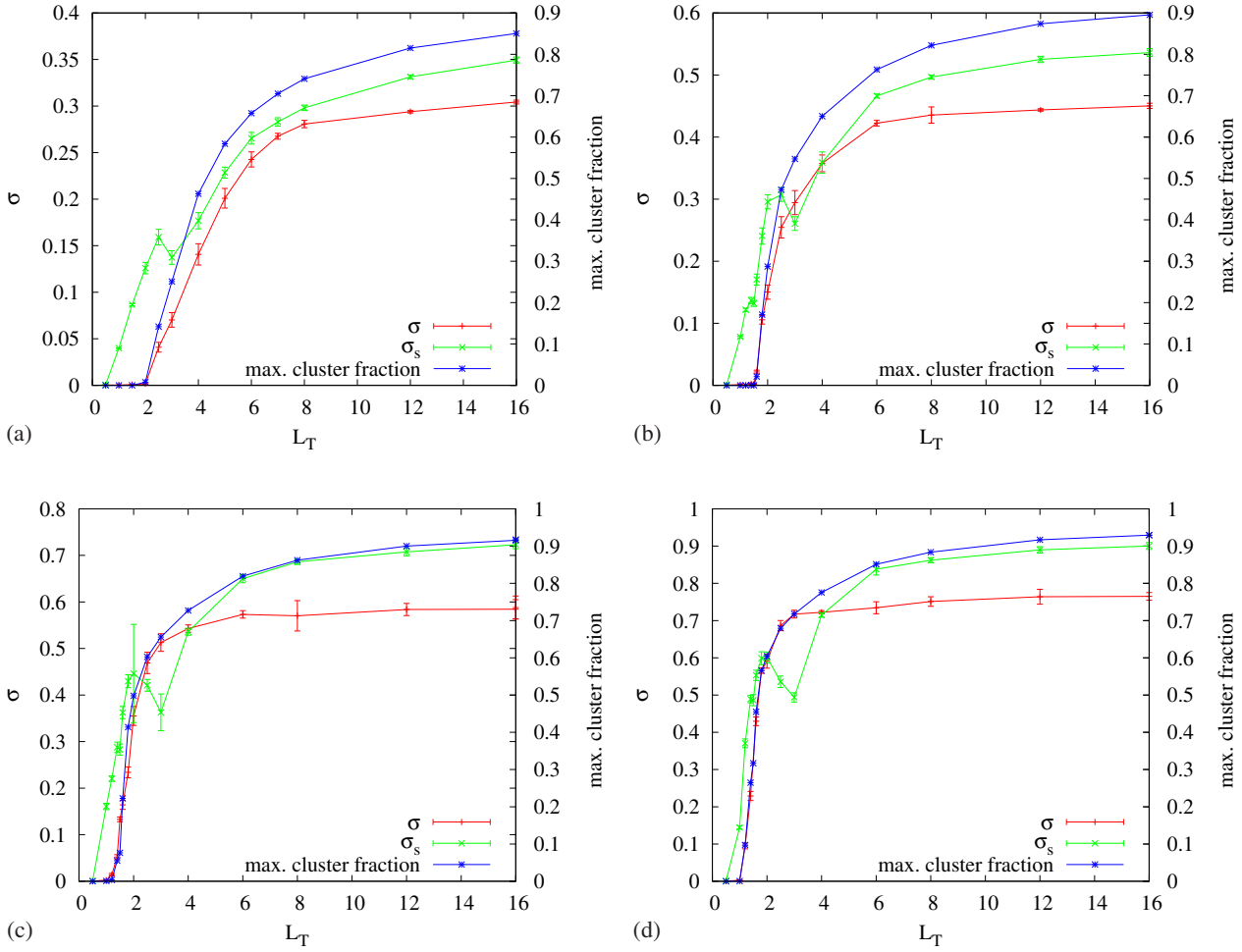

FIG. 9. Maximal cluster fraction, temporal and spatial string tensions σ and σ_s for density cutoff (a) $\rho = 6$, (b) $\rho = 8$, (c) $\rho = 10$, (d) $\rho = 12$ on $16^2 \times L_T$ volumes with vortex lengths $L_{\max} = 1.7$ and $L_{\min} = 0.3$.

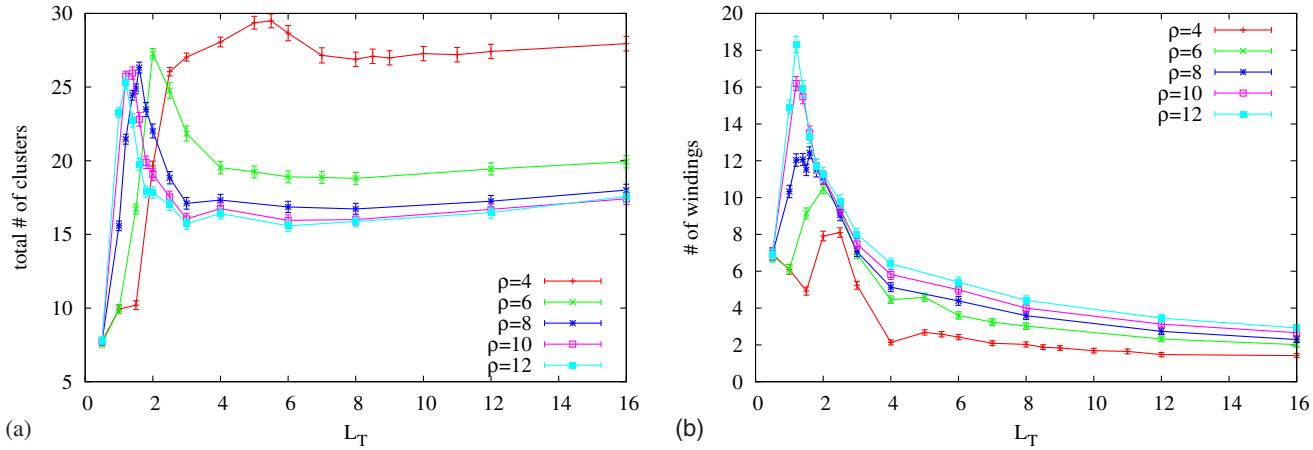

FIG. 10. (a) Total number of vortex clusters and (b) windings around the temporal dimension, for $16^2 \times L_T$ volumes, vortex lengths $L_{\max} = 1.7$ and $L_{\min} = 0.3$.

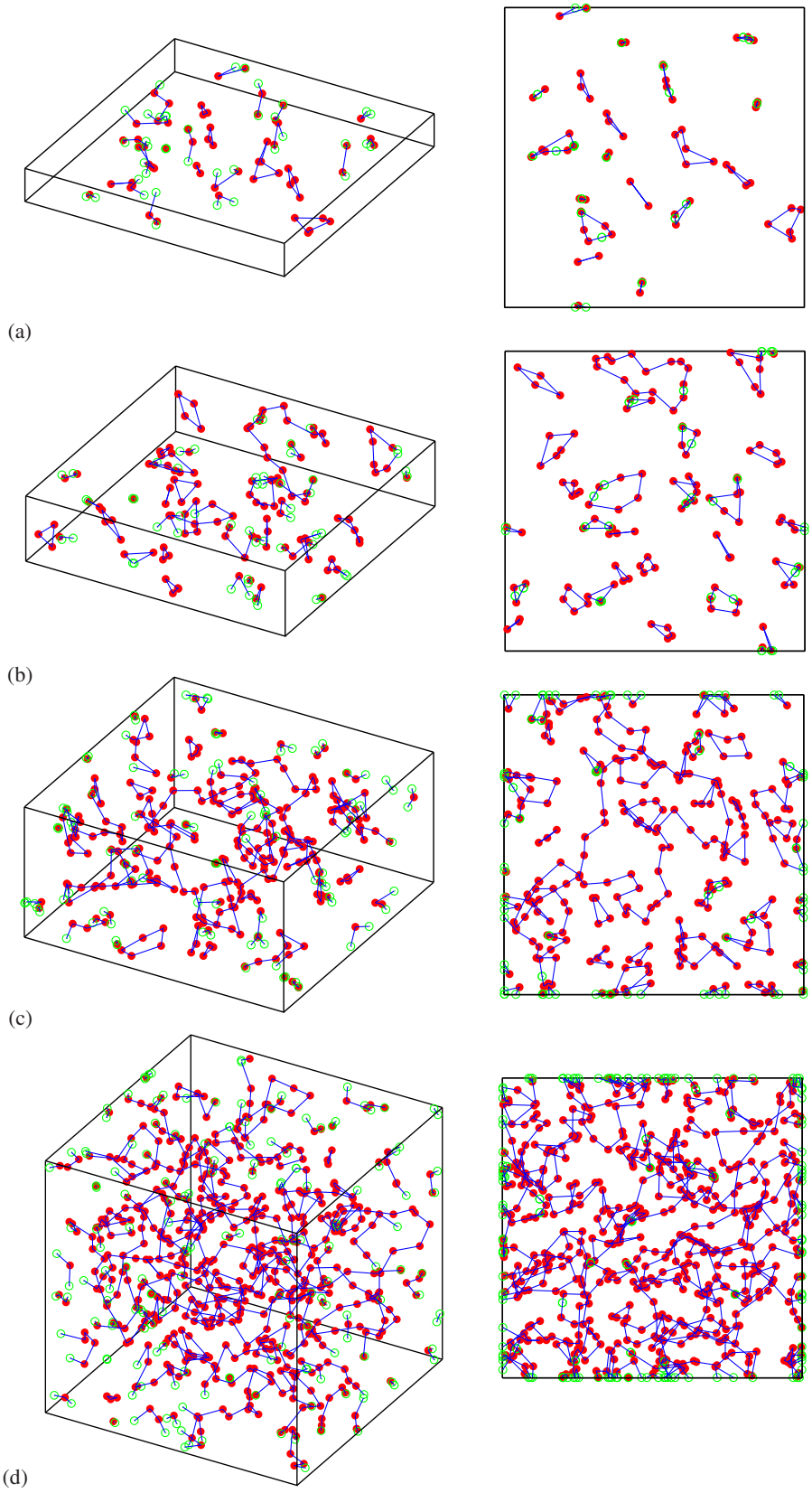

FIG. 11. Sample configurations on $16^2 \times L_T$ volumes for (a) $L_T = 2$, (b) $L_T = 4$, (c) $L_T = 8$, (d) $L_T = 16$ with density cutoff $\rho = 4$ and vortex lengths $L_{\max} = 1.7$ and $L_{\min} = 0.3$.

B. Deconfining transition as a function of vortex density cutoff ρ

In this section, we investigate the random vortex line ensembles for varying density cutoff $\rho = 4\ldots13$ on three different physical volumes $16^2 \times L_T$ with $L_T = 2\ldots4$, $L_{\max} = 1.7$, and $L_{\min} = 0.3$. In Fig. 12, we show the quark-antiquark potentials on a $16^2 \times 2$ volume, as well as the string tensions σ and σ_s and the maximal vortex cluster fraction as a function of ρ for the various L_T. In Fig. 13, we show the corresponding cluster size histograms. We observe a deconfinement transition with respect to the vortex density cutoff ρ. At $\rho = 4$, all cases are in the deconfined phase; the $L_T = 4$ configurations then immediately start to confine when ρ is increased, whereas the $L_T = 3$ and $L_T = 2$ configurations reach the transition around $\rho = 5$ and $\rho = 6$, respectively. Again, the confinement and percolation transitions [Fig. 12(b) and 12(d)] agree perfectly; the maximal clusters in Fig. 13 start to develop at exactly the aforementioned critical densities. Higher densities of course allow for more reconnections and percolation; i.e., they facilitate confinement. The spatial string tension at $\rho = 4$ essentially vanishes in the $L_T = 4$ case with percolation having ceased and almost no winding vortex clusters present to counteract the decline; on the other hand, for $L_T = 3$ and $L_T = 2$, the effect of winding vortices already manifests itself at $\rho = 4$ in a stabilization of the spatial string tension at finite values. This interplay was discussed in more detail already in the previous section.

C. Phase transition from varying maximal vortex length $L_{\max}$

In this section, we investigate the behavior of the ensembles at different maximal vortex segment lengths $L_{\max} = 1.0\ldots2.2$ for a physical volume $16^2 \times 2$ and a density cutoff $\rho = 8$, with $L_{\min} = 0.3$. In Fig. 14, we show the cluster size histogram, the quark-antiquark potential, and string tensions σ and σ_s as well as maximal cluster fraction vs the different maximal vortex segment lengths $L_{\max}$.

In this case, we observe a well-defined phase transition at $L_{\max} = 1.5$. There is no percolation and zero string tension σ, i.e., a flat quark-antiquark potential, below that threshold. At $L_{\max} = 1.5$ the maximal cluster fraction and string tension σ start to rise, hence percolation and confinement

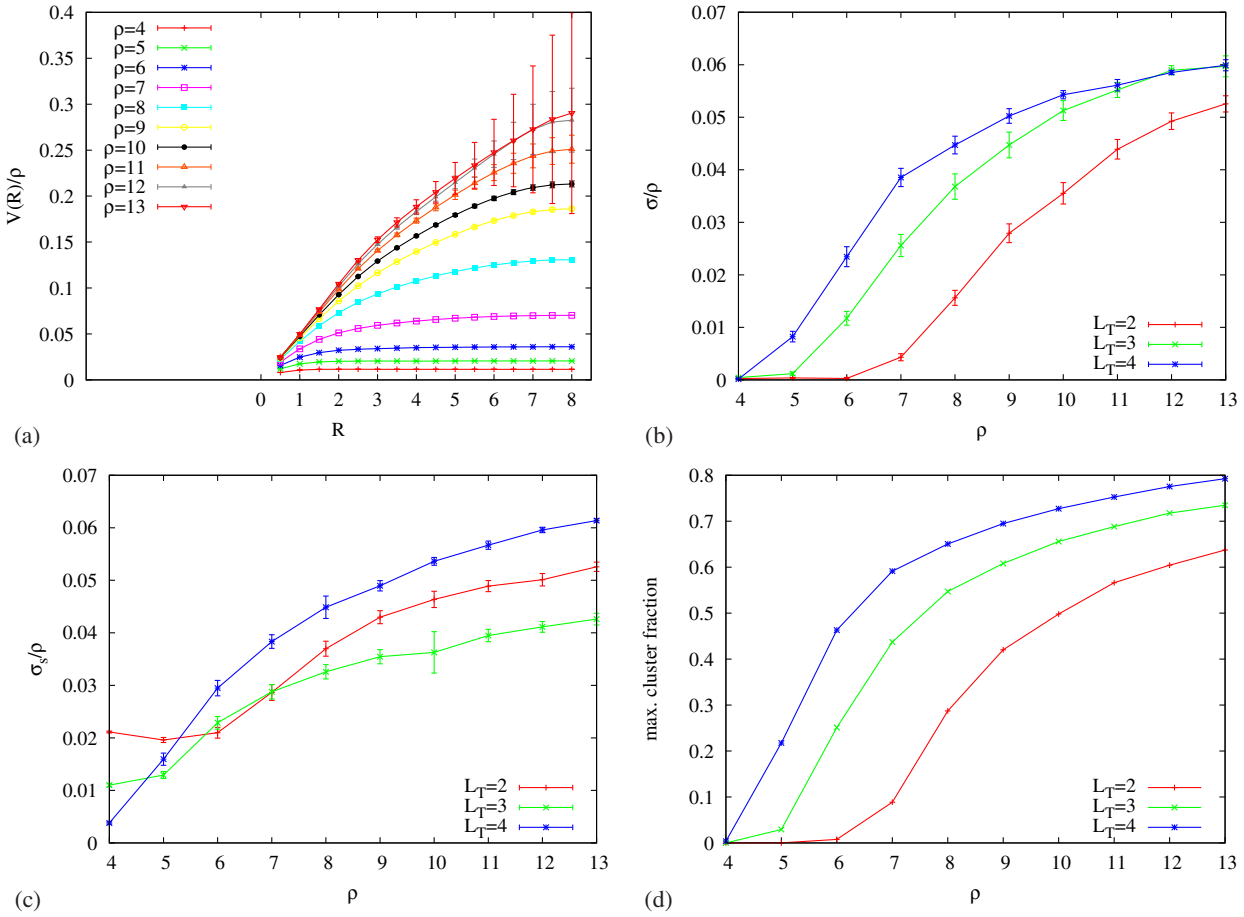

FIG. 12. (a) Quark-antiquark potentials on a $16^2 \times 2$ volume, string tensions (b) σ, (c) σ_s, and (d) maximal vortex cluster fraction as a function of density cutoff ρ for $16^2 \times L_T$ volumes and vortex lengths $L_{\max} = 1.7$, $L_{\min} = 0.3$.

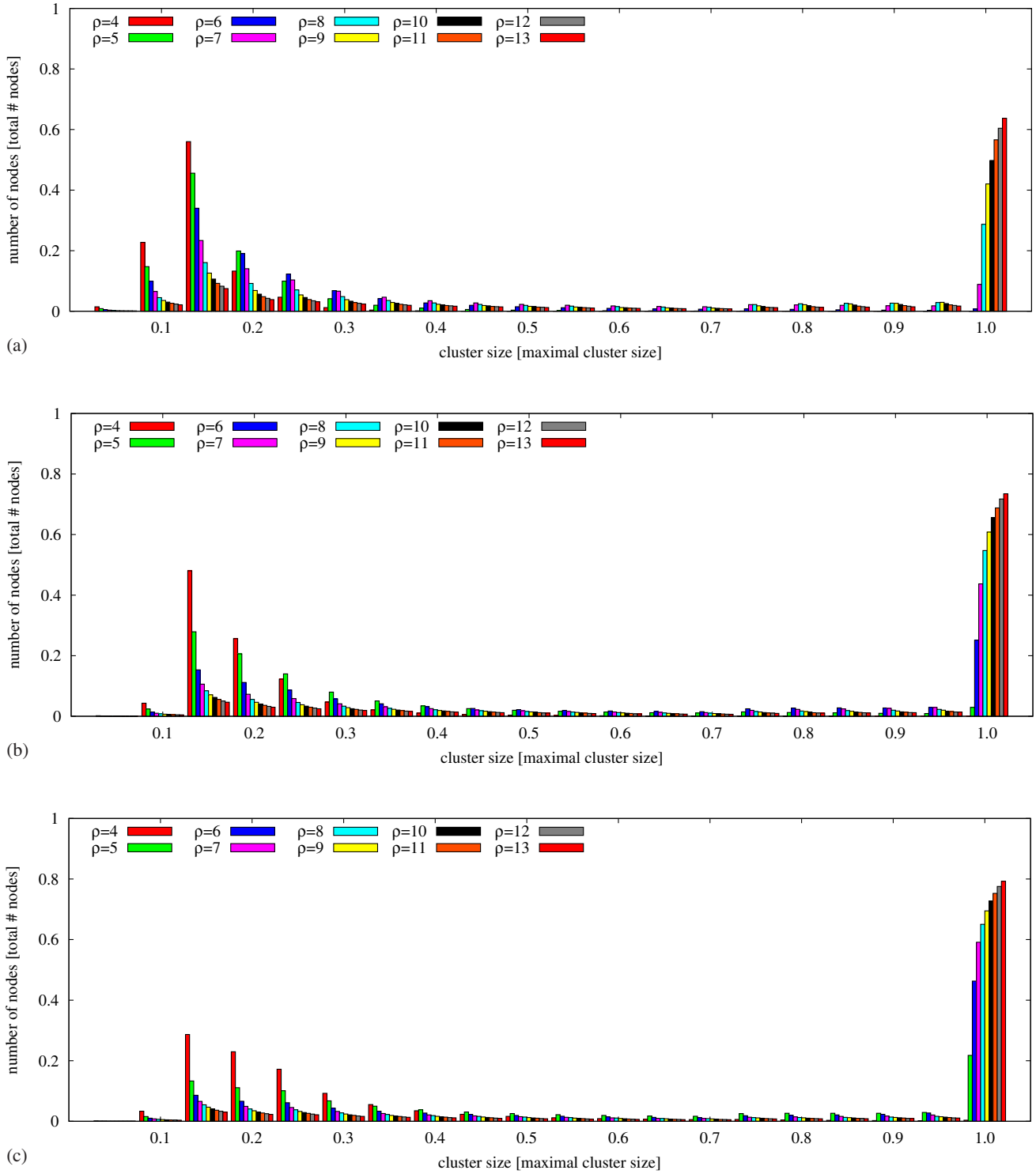

FIG. 13. Cluster size histograms on $16^2 \times L_T$ volumes for (a) $L_T = 2$, (b) $L_T = 3$, (c) $L_T = 4$ and different density cutoffs $\rho = 4 - 13$ with vortex lengths $L_{\max} = 1.7$ and $L_{\min} = 0.3$.

set in. Restricting the vortex line segment length to a more stringent upper bound shifts the action-entropy balance away from the entropy-dominated regime and leads to small, separated vortex clusters which cannot reconnect or percolate, and confinement is lost. Evidently, also the spatial string tension in the deconfined phase decreases as the $L_{\max}$ bound becomes more stringent, indicating that the number of vortices winding in the time direction is likewise suppressed.

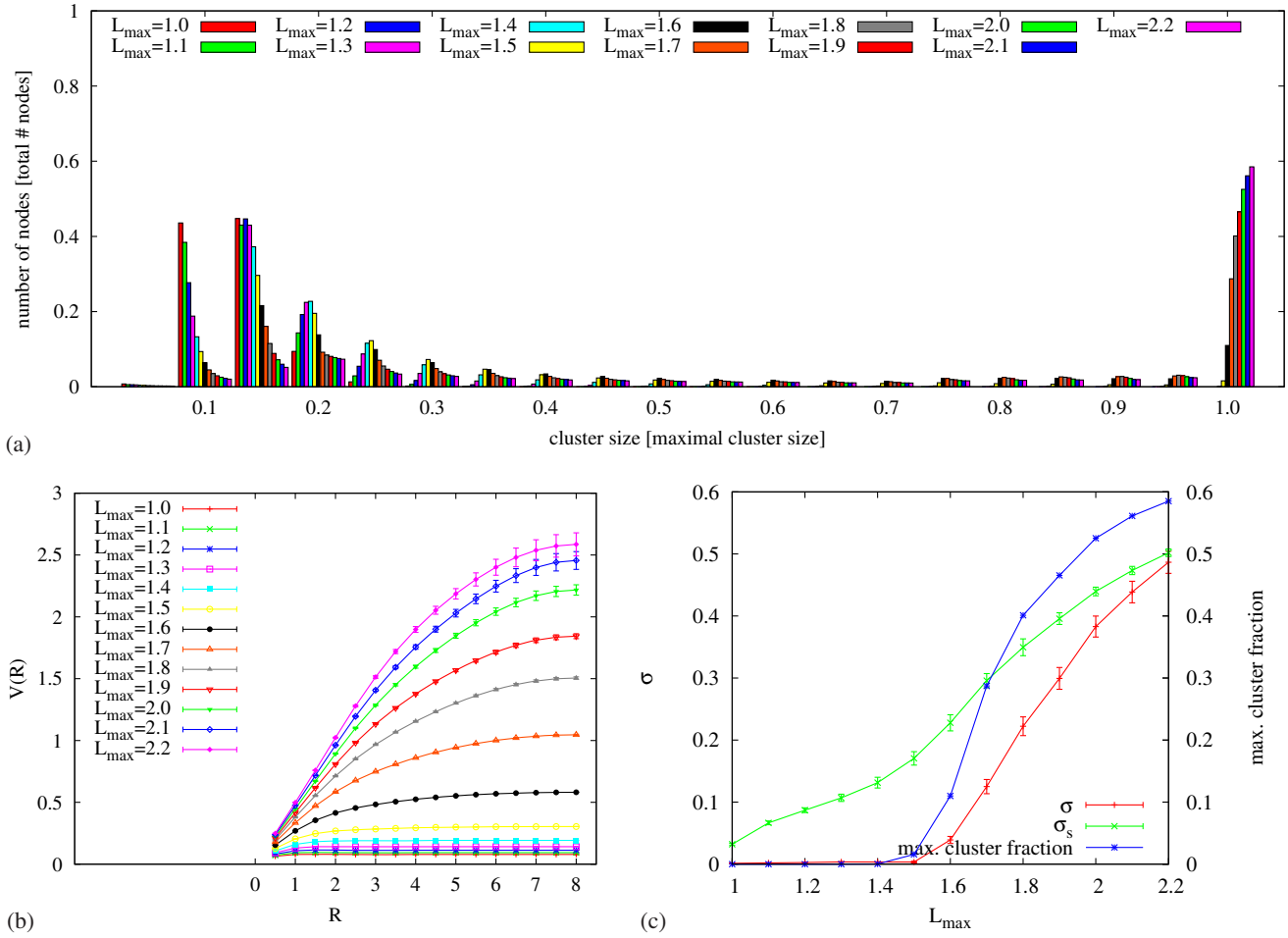

FIG. 14. (a) Cluster size histogram, (b) quark-antiquark potential, and (c) string tensions σ and σ_s as well as maximal cluster fraction as a function of maximal vortex segment length $L_{\max}$, for a $16^2 \times 2$ volume, density cutoff $\rho = 8$, and $L_{\min} = 0.3$.

D. Behavior as a function of minimal vortex/reconnection length $L_{\min}$

The interpretation of the phase space with respect to the minimal vortex segment length $L_{\min}$ is more complex than with respect to other parameters. $L_{\min}$ defines a minimal length scale which enters a number of effects governing the vortices; it not only restricts the minimal length of a vortex segment itself but also determines the maximal move radius $r_m = 4L_{\min}$, the maximal add radius $r_a = 3L_{\min}$, and the reconnection distance $r_r = L_{\min}$. That means that if we choose a small $L_{\min}$ the vortex clusters will not spread out quickly, and reconnections are strongly suppressed.

On the other hand, a large $L_{\min}$ restricts the set of available configurations and thus drives the system away from the entropy-dominated regime, while at the same time obstructing equilibration, with large attempted updates and frequent recombinations. Both limits do not realize the physical behavior we want to study, and our analysis of configurations in $16^2 \times 2$ volumes with vortex density $\rho = 8$, maximal vortex length $L_{\max} = 1.7$, and varying $L_{\min}$ seems to confirm these expectations. The aforementioned set of fixed parameters lies close to the critical point for all the deconfining phase transitions studied further above, i.e., as a function of temperature, vortex density, and maximal vortex segment length $L_{\max}$. In Fig. 15, we plot the cluster size histogram, the quark-antiquark potentials, string tensions σ and σ_s, and maximal cluster fraction as well as average vortex node action and vortex density vs $L_{\min} = 0.1 \ldots 0.7$ in steps of 0.05. We observe deconfined phases for both very small and very large $L_{\min}$. In the former case, the configurations remain rather static and do not readily recombine and percolate; in the latter case, the space of configurations is restricted, leading to a suppressed vortex density which also does not exhibit good percolation properties. At $L_{\min} = 0.3$, however, we find a common maximum for string tensions, maximal cluster fraction, and average vortex density, and simultaneously the average action shows a minimum. This validates our initial choice for $L_{\min} = 0.3$, which appears to yield rather stable ensembles that permitted reliable studies of the phase transitions investigated further above.

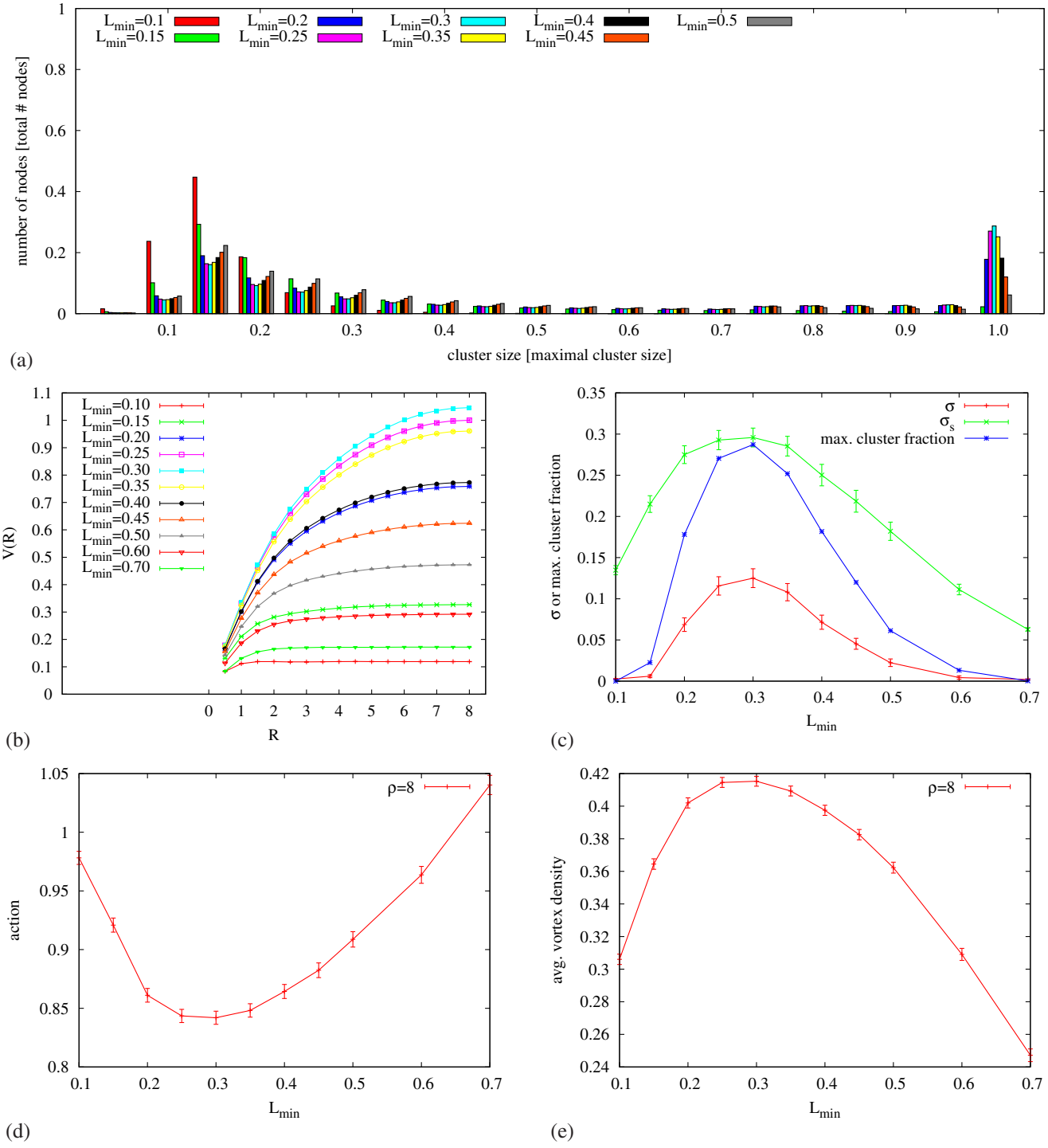

FIG. 15. (a) Cluster size histogram, (b) quark-antiquark potential, (c) string tensions and maximal vortex cluster fraction, average (d) node action, and (e) vortex line density (= avg. node density × avg. vortex length) for $16^2 \times 2$ volumes, density cutoff $\rho = 8$, and different vortex/reconnection lengths $L_{\min}$ at $L_{\max} = 1.7$.

E. Finite size analysis

We did not perform a systematic study of scaling with the spatial extent L_S, but comparison of selected results at $L_S = 16$ and $L_S = 32$ revealed no significant discrepancies. For example, we show in Fig. 16 the quark-antiquark potential $V(R, T = 1.5)$ from Wilson loops with temporal extent $T = 1.5$ and the string tension σ saturating with temporal extent of Wilson loops T, for $16^2 \times 8$ and $32^2 \times 8$ volumes with density cutoff $\rho = 8$ and vortex segment lengths $L_{\max} = 1.7$ and $L_{\min} = 0.3$. The results are compatible within errors; for the string tension, we obtain $\sigma = 0.438$ and $\sigma = 0.446$ on the smaller and larger volumes,

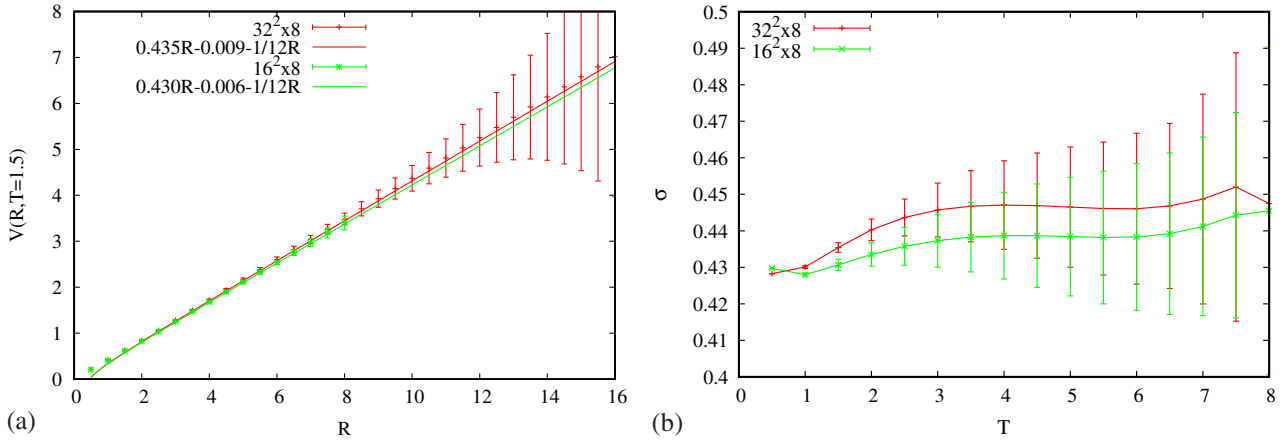

FIG. 16. (a) Quark-antiquark potential $V(R, T = 1.5)$ and (b) string tension σ saturating with temporal extent of Wilson loops T, for $16^2 \times 8$ and $32^2 \times 8$ volumes, density cutoff $\rho = 8$, $L_{\max} = 1.7$, and $L_{\min} = 0.3$.

respectively, which is a discrepancy of less than 2% at about 5% statistical uncertainties. Similar results were found for other observables, and therefore we conclude that finite size effects are under control.

V. CONCLUSIONS AND OUTLOOK

We presented a $2 + 1$-dimensional center vortex model of the Yang-Mills vacuum. The vortices are represented by closed random lines which are modeled as being piecewise linear, and an ensemble is generated by Monte Carlo methods. The physical space in which the vortex lines are defined is a torus with periodic boundary conditions. The motivation for this study was to explore a formulation which avoids the shortcomings of previous realizations of random center vortex models that relied on a hypercubic scaffolding for the construction of the vortex configurations. The present formulation preserves translational and rotational symmetry, and updates can occur continuously in space-time. Vortex configurations are allowed to grow and shrink, and also reconnections are allowed; i.e., vortex lines may fuse or disconnect. Our ensemble therefore contains not a fixed but a variable number of closed vortex lines. This is in fact a crucial ingredient for achieving a system of percolating vortices, i.e., a confining phase. All vortex updates (move, add, delete, and reconnect) are subjected to a Metropolis algorithm driven by an action depending on vortex segment length and the angle between two adjacent vortex segments; i.e., the action contains both a length and a curvature term. After tuning all necessary parameters, which are summarized in Sec. II C, we use the model to study both vortex percolation and the potential $V(R)$ between quark and antiquark as a function of distance R at different vortex densities, vortex segment length ranges, reconnection conditions, and different temperatures (by varying the temporal extent of the physical volume).

We have found three deconfinement transitions, namely, as a function of density, as a function of vortex segment length range, and as a function of temperature. The deconfinement transitions coincide with percolation transitions in the vortex configurations. For small vortex densities and restricted vortex segment lengths, the configurations consist of small, independent vortex clusters, and for high temperatures, vortex clusters prefer to separate and wind around the (short) temporal extent of the volume; in these cases, there is no percolation, the quark-antiquark potentials show no linearly rising behavior, i.e., no string tension is measured, and the system is in the deconfined phase. Once one allows for higher vortex densities, less restricted vortex segment lengths, or larger temporal extent, i.e., lower temperature, the vortex configurations begin to percolate; small clusters reconnect to mainly one large vortex cluster filling the whole volume. In this regime, we measure a finite string tension, i.e., linearly rising quark-antiquark potentials; hence, the vortices confine quarks and antiquarks.

The physically most relevant extension of the modeling effort presented here is of course the one to $D = 4$ space-time dimensions, where center vortices are described by two-dimensional random world surfaces. The surfaces can be represented by random triangulations, anchored again by nodes which can move, be added, or deleted from configurations. Surface separation at bottlenecks, and the converse process of the fusing of surfaces constitute crucial ingredients for achieving percolating configurations. In these $D = 4$ ensembles, one can then model Yang-Mills topological properties in addition to the confinement properties. A sobering lesson of the present exploratory study is the proliferation of modeling parameters in the type of formulation investigated here, compared to previous models utilizing a hypercubic scaffolding. This of course restricts the predictive potential of such models. Nevertheless, it has proven possible to reproduce the

qualitative features of confinement physics seen in $SU(2)$ Yang-Mills theory within the formulation constructed here.

In addition, extensions of the model to the $SU(3)$ and higher $SU(N)$ gauge groups can be envisioned. For more than two colors, vortices can branch, and one would need to introduce a generalized move update in which only part of the flux runs through the new path, and the rest stays on the old path. There would be more than one type of flux, i.e., $N-1$ types for $SU(N)$; one would need to keep track of how much flux is carried by each vortex segment. The implementation of higher N, just like the construction of higher-dimensional versions, would of course require entirely new tuning of the model parameters.

ACKNOWLEDGMENTS

We thank S. Catterall and D. A. Johnston for helpful discussions. This research was supported by the U.S. DOE through Grant No. DE-FG02-96ER40965 (D. A. and M. E.) and the Erwin Schrödinger Fellowship program of the Austrian Science Fund FWF ("Fonds zur Förderung der wissenschaftlichen Forschung") under Contract No. J3425-N27 (R. H.).

[1] G. 't Hooft, On the phase transition towards permanent quark confinement, Nucl. Phys. **B138**, 1 (1978).
[2] P. Vinciarelli, Fluxon solutions in non-Abelian gauge models, Phys. Lett. **78B**, 485 (1978).
[3] T. Yoneya, Z(n) topological excitations in Yang-Mills theories: Duality and confinement, Nucl. Phys. **B144**, 195 (1978).
[4] J. M. Cornwall, Quark confinement and vortices in massive gauge invariant QCD, Nucl. Phys. **B157**, 392 (1979).
[5] G. Mack and V. B. Petkova, Comparison of lattice gauge theories with gauge groups Z_2 and SU(2), Ann. Phys. **123**, 442 (1979).
[6] H. B. Nielsen and P. Olesen, A quantum liquid model for the QCD vacuum: Gauge and rotational invariance of domained and quantized homogeneous color fields, Nucl. Phys. **B160**, 380 (1979).
[7] L. Del Debbio, M. Faber, J. Greensite, and Š. Olejník, Center dominance and Z(2) vortices in SU(2) lattice gauge theory, Phys. Rev. D **55**, 2298 (1997).
[8] K. Langfeld, H. Reinhardt, and O. Tennert, Confinement and scaling of the vortex vacuum of SU(2) lattice gauge theory, Phys. Lett. B **419**, 317 (1998).
[9] L. Del Debbio, and M. Faber, and J. Greensite, and Š. Olejník, Center dominance, center vortices, and confinement, arXiv:hep-th/9708023.
[10] K. Langfeld, O. Tennert, M. Engelhardt, and H. Reinhardt, Center vortices of Yang-Mills theory at finite temperatures, Phys. Lett. B **452**, 301 (1999).
[11] T. G. Kovacs and E. T. Tomboulis, Vortices and confinement at weak coupling, Phys. Rev. D **57**, 4054 (1998).
[12] M. Engelhardt and H. Reinhardt, Center vortex model for the infrared sector of Yang-Mills theory: Confinement and deconfinement, Nucl. Phys. **B585**, 591 (2000).
[13] M. Engelhardt, K. Langfeld, H. Reinhardt, and O. Tennert, Deconfinement in SU(2) Yang-Mills theory as a center vortex percolation transition, Phys. Rev. D **61**, 054504 (2000).
[14] R. Bertle and M. Faber, Vortices, confinement and Higgs fields, arXiv:hep-th/0212027.
[15] M. Engelhardt, M. Quandt, and H. Reinhardt, Center vortex model for the infrared sector of SU(3) Yang-Mills theory: Confinement and deconfinement, Nucl. Phys. **B685**, 227 (2004).
[16] A. L. L. de Lemos, L. E. Oxman, and B. F. I. Teixeira, Derivation of an Abelian effective model for instanton chains in 3D Yang-Mills theory, Phys. Rev. D **85**, 125014 (2012).
[17] L. E. Oxman, Confinement of quarks and valence gluons in SU(N) Yang-Mills-Higgs models, J. High Energy Phys. 03 (2013) 038.
[18] R. Höllwieser, D. Altarawneh, and M. Engelhardt, Random center vortex lines in continuous 3D space-time, AIP Conf. Proc. **1701**, 030007 (2016).
[19] D. Altarawneh, R. Höllwieser, and M. Engelhardt, Confining bond rearrangement in random center vortex models, Phys. Rev. D **93**, 054007 (2016).
[20] R. Höllwieser and D. Altarawneh, Center vortices, area law and the catenary solution, Int. J. Mod. Phys. A **30**, 1550207 (2015).
[21] J. Greensite, The confinement problem in lattice gauge theory, Prog. Part. Nucl. Phys. **51**, 1 (2003).
[22] J. Greensite and R. Höllwieser, Double-winding Wilson loops and monopole confinement mechanisms, Phys. Rev. D **91**, 054509 (2015).
[23] R. Bertle, M. Engelhardt, and M. Faber, Topological susceptibility of Yang-Mills center projection vortices, Phys. Rev. D **64**, 074504 (2001).
[24] M. Engelhardt, Center vortex model for the infrared sector of Yang-Mills theory: Topological susceptibility, Nucl. Phys. **B585**, 614 (2000).
[25] M. Engelhardt, Center vortex model for the infrared sector of SU(3) Yang-Mills theory: Topological susceptibility, Phys. Rev. D **83**, 025015 (2011).
[26] R. Höllwieser, M. Faber, and U. M. Heller, Lattice index theorem and fractional topological charge, arXiv:1005.1015.
[27] R. Höllwieser, M. Faber, and U. M. Heller, Intersections of thick center vortices, dirac eigenmodes and fractional topological charge in SU(2) lattice gauge theory, J. High Energy Phys. 06 (2011) 052.
[28] T. Schweigler, R. Höllwieser, M. Faber, and U. M. Heller, Colorful SU(2) center vortices in the continuum and on the lattice, Phys. Rev. D **87**, 054504 (2013).

[29] R. Höllwieser, M. Faber, and U. M. Heller, Critical analysis of topological charge determination in the background of center vortices in SU(2) lattice gauge theory, Phys. Rev. D **86**, 014513 (2012).
[30] R. Höllwieser and M. Engelhardt, Smearing center vortices, Proc. Sci., LAT2014 (**2014**) 356.
[31] R. Höllwieser and M. Engelhardt, Approaching SU(2) gauge dynamics with smeared Z(2) vortices, Phys. Rev. D **92**, 034502 (2015).
[32] P. de Forcrand and M. D'Elia, On the relevance of center vortices to QCD, Phys. Rev. Lett. **82**, 4582 (1999).
[33] C. Alexandrou, P. de Forcrand, and M. D'Elia, The role of center vortices in QCD, Nucl. Phys. **A663**, 1031 (2000).
[34] M. Engelhardt and H. Reinhardt, Center projection vortices in continuum Yang-Mills theory, Nucl. Phys. **B567**, 249 (2000).
[35] H. Reinhardt and M. Engelhardt, *Center Vortices in Continuum Yang-Mills Theory, in Quark Confinement and the Hadron Spectrum IV*, edited by W. Lucha and K. M. Maung (World Scientific, Singapore, 2002), p. 150.
[36] M. Engelhardt, Center vortex model for the infrared sector of Yang-Mills theory: Quenched Dirac spectrum and chiral condensate, Nucl. Phys. **B638**, 81 (2002).
[37] D. B. Leinweber, P. O. Bowman, U. M. Heller, D.-J. Kusterer, K. Langfeld, and A. G. Williams, Role of centre vortices in dynamical mass generation, Nucl. Phys. B, Proc. Suppl. **161**, 130 (2006).
[38] V. G. Bornyakov, E.-M. Ilgenfritz, M. Müller-Preussker, B. V. Martemyanov, S. M. Morozov, and A. I. Veselov, Interrelation between monopoles, vortices, topological charge and chiral symmetry breaking: Analysis using overlap fermions for SU(2), Phys. Rev. D **77**, 074507 (2008).
[39] R. Höllwieser, M. Faber, J. Greensite, U. M. Heller, and Š. Olejník, Center vortices and the Dirac spectrum, Phys. Rev. D **78**, 054508 (2008).
[40] P. O. Bowman, K. Langfeld, D. B. Leinweber, A. Sternbeck, L. von Smekal, and A. G. Williams, Role of center vortices in chiral symmetry breaking in SU(3) gauge theory, Phys. Rev. D **84**, 034501 (2011).
[41] R. Höllwieser, T. Schweigler, M. Faber, and U. M. Heller, Center vortices and chiral symmetry breaking in SU(2) lattice gauge theory, Phys. Rev. D **88**, 114505 (2013).
[42] N. Brambilla *et al.*, QCD and strongly coupled gauge theories: Challenges and perspectives, Eur. Phys. J. C **74**, 2981 (2014).
[43] R. Höllwieser, M. Faber, Th. Schweigler, and U. M. Heller, Chiral symmetry breaking from center vortices, Proc. Sci., LAT2013 (**2014**) 505.
[44] D. Trewartha, W. Kamleh, and D. Leinweber, Centre vortex effects on the overlap quark propagator, Proc. Sci., LATTICE2014 (**2014**) 357.
[45] D. Trewartha, W. Kamleh, and D. Leinweber, Evidence that centre vortices underpin dynamical chiral symmetry breaking in SU(3) gauge theory, Phys. Lett. B **747**, 373 (2015).
[46] M. Quandt, H. Reinhardt, and M. Engelhardt, Center vortex model for the infrared sector of SU(3) Yang-Mills theory—vortex free energy, Phys. Rev. D **71**, 054026 (2005).
[47] M. Engelhardt, Center vortex model for the infrared sector of SU(3) Yang-Mills theory—baryonic potential, Phys. Rev. D **70**, 074004 (2004).
[48] M. Engelhardt, Center vortex model for the infrared sector of SU(4) Yang-Mills theory: String tensions and deconfinement transition, Phys. Rev. D **73**, 034015 (2006).
[49] M. Engelhardt and B. Sperisen, Center vortex model for Sp(2) Yang-Mills theory, Phys. Rev. D **74**, 125011 (2006).
[50] C. Baillie, D. Johnston, and R. Williams, Computational aspects of simulating dynamically triangulated random surfaces, Comput. Phys. Commun. **58**, 105 (1990).
[51] S. Catterall, Simulations of dynamically triangulated gravity—An algorithm for arbitrary dimension, Comput. Phys. Commun. **87**, 409 (1995).
[52] S. Jain and S. D. Mathur, World-sheet geometry and baby universes in 2-D quantum gravity, Phys. Lett. B **286**, 239 (1992).
[53] J. Ambjørn, S. Jain, and G. Thorleifsson, Baby universes in 2-d quantum gravity, Phys. Lett. B **307**, 34 (1993).
[54] G. Thorleifsson and S. Catterall, A real space renormalization group for random surfaces, Nucl. Phys. **B461**, 350 (1996).
[55] J. Ambjørn and J. Jurkiewicz, Scaling in four-dimensional quantum gravity, Nucl. Phys. **B451**, 643 (1995).